

CrossMark
click for updatesCite this: *J. Mater. Chem. A*, 2016, 4, 1319

Hierarchical carbon@Ni₃S₂@MoS₂ double core–shell nanorods for high-performance supercapacitors†

Laiquan Li,^{ab} Hongbin Yang,^b Jun Yang,^a Liping Zhang,^b Jianwei Miao,^b Yufei Zhang,^a Chencheng Sun,^a Wei Huang,^a Xiaochen Dong^{*a} and Bin Liu^{*b}

Hierarchical carbon@Ni₃S₂@MoS₂ (C@Ni₃S₂@MoS₂) double core–shell nanorods have been synthesized by a facile hydrothermal method using highly conductive carbon/Ni (C/Ni) nanorods as both the precursor and template. As supercapacitor electrodes, the C@Ni₃S₂@MoS₂ nanorods deliver a specific capacitance as high as 1544 F g⁻¹ at a current density of 2 A g⁻¹ with excellent cycling stability (retaining 92.8% of the capacitance after 2000 cycles at a current density of 20 A g⁻¹). The C/Ni nanorods as the backbone played crucial roles in enhancing the rate performance of the device, in the meanwhile, interconnected MoS₂ nanosheets on the shell provided numerous accessible surfaces and contacts with the electrolyte. Our work demonstrated an effective design of robust hierarchical double core/shell nanostructures, which could provide a general and promising approach to fabricate high-performance materials for energy storage applications.

Received 29th October 2015
Accepted 1st December 2015

DOI: 10.1039/c5ta08714g

www.rsc.org/MaterialsA

1. Introduction

The design of high-performance energy storage devices has become one of the most urgent challenges on the way to finding sustainable solutions to the energy crisis. Over the past few years, supercapacitors have received great attention in high-power applications because of their high energy density, fast charging/discharging rate, long cycle life, and excellent cycling stability.^{1–3} Great efforts have been devoted to developing high-capacity electrode materials and designing optimal electrode architectures to achieve better electrochemical performance.⁴

Transition metal sulfides are promising electrode materials for energy-related applications including fuel cells, lithium-ion batteries, and electrochemical capacitors because of their unique physical and chemical properties.^{5–7} Among them, nickel sulfides are attractive owing to their various valence states, low cost and excellent electrochemical performance. In particular, Ni₃S₂ with high theoretical specific capacitance has been applied in high-performance lithium-ion batteries^{8,9} and supercapacitors.^{10,11} However, the poor electrical conductivity and rate capability limit the practical use of Ni₃S₂.¹² Recently, it

was demonstrated that the electrochemical performance of Ni₃S₂ could be remarkably enhanced by combining Ni₃S₂ with conductive additives. For instance, Xing *et al.*¹³ reported a novel hierarchical ZnO@Ni₃S₂ nanostructure by electrodepositing Ni₃S₂ on ZnO nanorod arrays supported on Ni foam, which showed a high specific capacitance of 1529 F g⁻¹ at a current density of 2 A g⁻¹, while only 42% of the capacity remained after 2000 cycles. Lou *et al.*¹⁴ synthesized one-dimensional (1D) carbon nanotube@Ni₃S₂ nanostructures with good rate performance and excellent cycling durability (88% capacity retention after 1500 cycles), but only a small capacitance of 514 F g⁻¹ was delivered at a current density of 4 A g⁻¹. Until now, it is still challenging to realize both high capacitance and good cycling stability in Ni₃S₂-based supercapacitors.

Core–shell nanostructures with a tunable material composition and functionality could help to improve both the conductivity as well as charge storage capability in electrodes for energy storage devices.^{15–17} For example, a conductive core could enhance the charge conduction within the material, while a shell made of porous materials could provide better contact with ions at the electrode–electrolyte interface and buffer the volume change during the charge/discharge process.

Herein, we demonstrate a facile hydrothermal approach to prepare hierarchical C@Ni₃S₂@MoS₂ double core–shell nanorods using highly conductive C/Ni nanorods as both the structural support and nickel source. On one hand, the C/Ni nanorods could provide a highly conductive backbone for charge transport and storage, thus significantly improving the rate capability. On the other hand, the *in situ* formation of active materials (Ni₃S₂ and MoS₂) on C/Ni nanorods could

^aKey Laboratory of Flexible Electronics (KLOFE) & Institute of Advanced Materials (IAM), Jiangsu National Synergistic Innovation Center for Advanced Materials (SICAM), Nanjing Tech University (NanjingTech), 30 South Puzhu Road, Nanjing 211816, China. E-mail: Liubin@ntu.edu.sg; iamxcdong@njtech.edu.cn

^bSchool of Chemical and Biomedical Engineering, Nanyang Technological University, 62 Nanyang Drive, Singapore 637459, Singapore

† Electronic supplementary information (ESI) available. See DOI: 10.1039/c5ta08714g

increase the contact area with the electrolyte, and thus enhance the capacitance as well as protect the conductive core during fast reversible redox processes. Consequently, the C@Ni₃S₂@MoS₂ double core-shell nanorods showed a high specific capacitance as high as 1544 F g⁻¹ at a current density of 2 A g⁻¹ and greatly improved cyclic capacity retention (retaining 92.8% of the capacitance after 2000 cycles at a current density of 20 A g⁻¹) as electrodes in supercapacitors.

2. Experimental section

2.1 Preparation of C/Ni nanorods

All chemicals were purchased from Sigma-Aldrich and used without further purification. The C/Ni nanorods were synthesized based on a similar method reported in the literature.¹⁸ The synthesis of C/Ni-700 nanorods is schematically illustrated in Fig. S1.† In a typical synthesis, 0.278 g of dimethylglyoxime was dispersed into 24 mL of ethanol with pH adjusted to 13 using 0.5 M NaOH ethanolic solution. The mixture was then dropped into 700 mL of deionized water containing 0.521 g of NiCl₂·6H₂O under ultrasonication. Subsequently, the red cotton-like precipitate was collected and thoroughly washed with deionized water and absolute alcohol several times, followed by vacuum-drying at 80 °C for 6 h. The sample was then calcined in a N₂ atmosphere for 1 h at several carbonization temperatures, namely 300 °C, 500 °C, 700 °C and 900 °C, which were labeled as C/Ni-300, C/Ni-500, C/Ni-700 and C/Ni-900.

2.2 Synthesis of hierarchical C@Ni₃S₂@MoS₂ nanorods

20 mg of C/Ni nanorods and 20 mg of sodium dodecyl sulfate were added into 20 mL of deionized water under ultrasonication in 30 min. Then 24 mg of sodium molybdate (Na₂MoO₄·2H₂O) was added into the above solution and stirred to form a suspension. After adding 100 mg of L-cysteine, the mixture was then transferred into a 25 mL Teflon-lined stainless steel autoclave and heated at 200 °C for 24 h. To improve the crystallinity of MoS₂, the harvested black product was calcined at 400 °C in 5% H₂ balanced by Ar for 2 h at a heating rate of 5 °C min⁻¹. The final products synthesized from C/Ni nanorods with different carbonization temperatures were marked as C@NM-300, C@NM-500, C@NM-700 and C@NM-900. For comparison, carbon@Ni₃S₂ (C@Ni₃S₂) nanorods were synthesized under the same conditions without sodium molybdate. Meanwhile, C@MoS₂ nanorods were also prepared using acid-etched C/Ni-700 nanorods (2 M HCl, 80 °C, 10 h) as the precursor.

2.3 Characterization

The crystal structures were analyzed by using a X-ray diffractometer (XRD, Bruker AXS D8 Advance) with Cu Kα radiation (λ = 1.5406 Å). The morphological and lattice structural information were examined with a field-emission scanning electron microscope (FESEM, JEOL, JSM6700F) and transmission electron microscope (TEM, FEI Tecnai G230). The surface area was measured by nitrogen adsorption-desorption at 77 K, using the Brunauer-Emmett-Teller (BET) method. The nickel content in C/Ni nanorods was studied by thermogravimetric

analysis, which was performed from 25 to 800 °C at a heating rate of 10 °C min⁻¹ under air atmosphere (TGA, Diamond TG/DTA, Perkin Elmer, MA, USA). The nature of carbon in C/Ni nanorods was examined by using a Raman microscope (Renishaw RM1000), with a 514.5 nm excitation laser. Combustion analysis was conducted on a Vario EL III CHNS Elemental Analyzer (EA).

2.4 Electrochemical measurements

Electrochemical measurements were carried out on a CHI 760D electrochemical workstation (CH Instruments) with a saturated Ag/AgCl as the reference electrode and a Pt plate as the counter electrode. 6.0 M KOH aqueous solution was used as the electrolyte. To prepare the working electrodes, the C@Ni₃S₂@MoS₂ nanorods, acetylene black and PVDF were used as the active material, conductive agent and binder with a weight ratio of 7 : 2 : 1, respectively. The electrode paste was coated onto nickel foam with a calculated mass loading of around 1.0 mg. The electrochemical performance of the supercapacitor was evaluated by cyclic voltammetry (CV), galvanostatic charge-discharge tests, and electrochemical impedance spectroscopy (EIS) measurements (1 to 10⁵ Hz).

3. Results and discussion

Fig. 1 displays a schematic illustration to summarize the formation of the C@Ni₃S₂@MoS₂ double core-shell nanorods. The precursor C/Ni nanorods played a dual role in the synthesis, which not only acted as the 1D template, but also provided the nickel source for the growth of Ni₃S₂. During the synthesis, L-cysteine decomposed and released S²⁻ ions, which acted as the S source as well as the reducing agent for the formation of MoS₂. Meanwhile, S²⁻ ions reacted with the Ni nanoparticles on the surface of C/Ni nanorods to *in situ* form Ni₃S₂ (eqn (1)). Sodium dodecyl sulfate (SDS) was used as the surfactant to provide sulfonic acid groups (SO₃⁻), which uniformly distributed on the surface of C/Ni nanorods. The Mo precursor could adsorb on the surface of C/Ni nanorods owing to the strong hydrogen-bond interaction between sulfonic acid groups and MoO₄²⁻ to form MoS₂ by reacting with S²⁻ ions (eqn (2)).¹⁹

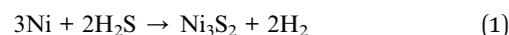


Fig. 1 Schematic illustration to show the formation of C@Ni₃S₂@MoS₂ nanorods.

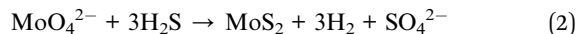


Fig. 2a shows the XRD pattern of the precursor C/Ni-700 nanorods. The two distinct diffraction peaks at 44.4° and 51.8° can be attributed to the (111) and (200) planes of metallic nickel (JCPDS card no. 04-0850). The broad peak at about 26° corresponds to the (002) plane of carbon,²⁰ which originates from carbonization of the nickel dimethylglyoxime. During the hydrothermal synthesis, S^{2-} ions were released from the decomposition of *L*-cysteine, which reacted with nickel particles fixed on the surface of the C/Ni nanorods to form Ni_3S_2 . As shown in Fig. 2b, obvious diffraction peaks corresponding to Ni_3S_2 (JCPDS card no. 44-1418) are observable. When sodium molybdate was further added during the synthesis, the final product contains both Ni_3S_2 and MoS_2 (JCPDS card no. 37-1492) (Fig. 2c).

The morphology and detailed crystal structure of the products were investigated by field-emission scanning electron microscopy (FESEM) and transmission electron microscopy (TEM). Fig. 3a shows the FESEM image of the precursor C/Ni-700, which has a rod-like structure with a diameter of 200–300 nm and a length of about 5 μm . It is clear to see that small nickel nanoparticles are uniformly distributed on the surface, which is further confirmed by using TEM images (Fig. 3d). The high-resolution TEM (HR-TEM) image as shown in the inset of Fig. 3d reveals clear lattice spacing corresponding to the (111) plane of metallic nickel. The weight ratio of nickel in C/Ni nanorods was calculated to be 52.8% (Fig. S2†). After hydrothermal synthesis, as shown in Fig. 3b, Ni_3S_2 nanoparticles are found to be distributed uniformly on the carbon network backbones. The TEM image of the C@ Ni_3S_2 nanorods (Fig. 3e) shows that the Ni_3S_2 nanoparticles have diameters of 20 to 40 nm. The inset in Fig. 3e shows the HR-TEM image, in which the interplanar spacing corresponding to (110) and (003) planes of hexagonal Ni_3S_2 are clearly visible. Fig. 3c displays the FESEM image of the C@ Ni_3S_2 @ MoS_2 double core-shell nanorods.

From which, it can be seen that the entire surface of the carbon backbone is uniformly covered with interconnected MoS_2 nanosheets. Both MoS_2 nanosheets and Ni_3S_2 nanoparticles are detected in the TEM image as shown in Fig. 3f. The MoS_2 nanosheets have an average thickness of 50 nm, growing tightly on the inner carbon backbones. Fig. 3g shows the HRTEM image obtained from the red dotted region in Fig. 3f. The lattice spacing of 0.28 nm is assigned to the (110) interplanar spacing of hexagonal Ni_3S_2 . Meanwhile, the lattice spacing of 0.62 nm and 0.27 nm are attributed to the (002) and (100) planes of MoS_2 . The C@ Ni_3S_2 @ MoS_2 nanorods were further examined by energy dispersive X-ray spectroscopy (EDX) elemental mapping as displayed in Fig. 3h–l. Both nickel and molybdenum signals are observed to be uniformly distributed on the shell of the nanorods. By overlapping the nickel and molybdenum signals, it is found that MoS_2 sits on the outer shell with a thickness of about 50 nm, consistent with our previous FESEM and TEM measurements (Fig. 3c and f). Additionally, the carbon backbone is also detected in the inner core (Fig. S3†). To study the composition of the C@ Ni_3S_2 @ MoS_2 nanorods, TGA and combustion analysis were carried out as shown in Fig. S4 and Table S3.† The oxidation of carbon with a weight loss of 17.2% occurs at around 350°C , which is consistent with the combustion analysis (Table S3†) and the TGA curve of C/Ni-700 (Fig. S2†). The second weight loss ($400\text{--}500^\circ\text{C}$) is assigned to the oxidation of MoS_2 .^{21,22} The third weight loss in the temperature range from 660°C to 740°C is due to the oxidation of Ni_3S_2 .²³ Based on the weight loss, the weight ratio of Ni_3S_2 and MoS_2 was estimated to be 64.8% and 28.7%, respectively. The relative low weight percentage of MoS_2 is consistent with the thin shell of the composite. Additionally, the combustion analysis shows a similar weight ratio of C and S among the C@NM-300, C@NM-500, C@NM-700 and C@NM-900 samples, indicating no obvious composition change with increasing graphitization temperature of the C/Ni nanorods.

The electrochemical behavior of the core-shell nanorods was evaluated using cyclic voltammetry (CV) and galvanostatic charging–discharging techniques. Fig. 4a shows the CV curves of C@NM-300, C@NM-500, C@NM-700 and C@NM-900 recorded at a scan rate of 25 mV s^{-1} . All CV curves exhibit a pair of redox peaks, indicating a typical pseudocapacitive behavior. The galvanostatic charging–discharging curves of C@NM-300, C@NM-500, C@NM-700, and C@NM-900 are shown in Fig. 4b, with their corresponding current density dependent specific capacitance plotted in Fig. 4c. The specific capacitance was calculated based on eqn (3):²⁴

$$C = I \times \Delta t / (m \times \Delta V) \quad (3)$$

where C (F g^{-1}) is the specific capacitance, I (A) is the discharge current, Δt (s) is the discharge time, m (g) is the mass of the active material, and ΔV (V) is the potential window for the charge–discharge process. Among various tested samples, the C@NM-700 exhibits the highest specific capacitance of 1544, 1500, 1404, 1388, 1327, 1280, 1192 and 1170 F g^{-1} at current densities of 2, 4, 8, 10, 15, 20, 30 and 40 A g^{-1} , respectively. For comparison, the specific capacitance of C@NM-300, C@NM-

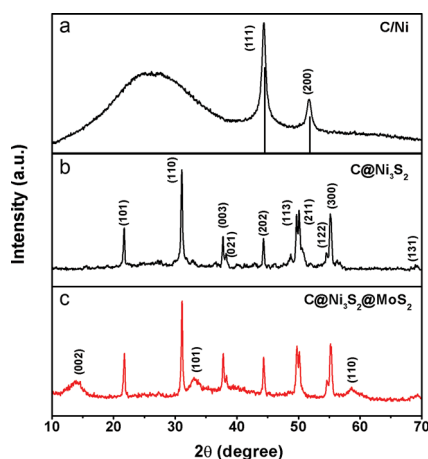


Fig. 2 XRD patterns of (a) C/Ni-700 nanorods, (b) C@ Ni_3S_2 core-shell nanorods, and (c) hierarchical C@ Ni_3S_2 @ MoS_2 double core-shell nanorods.

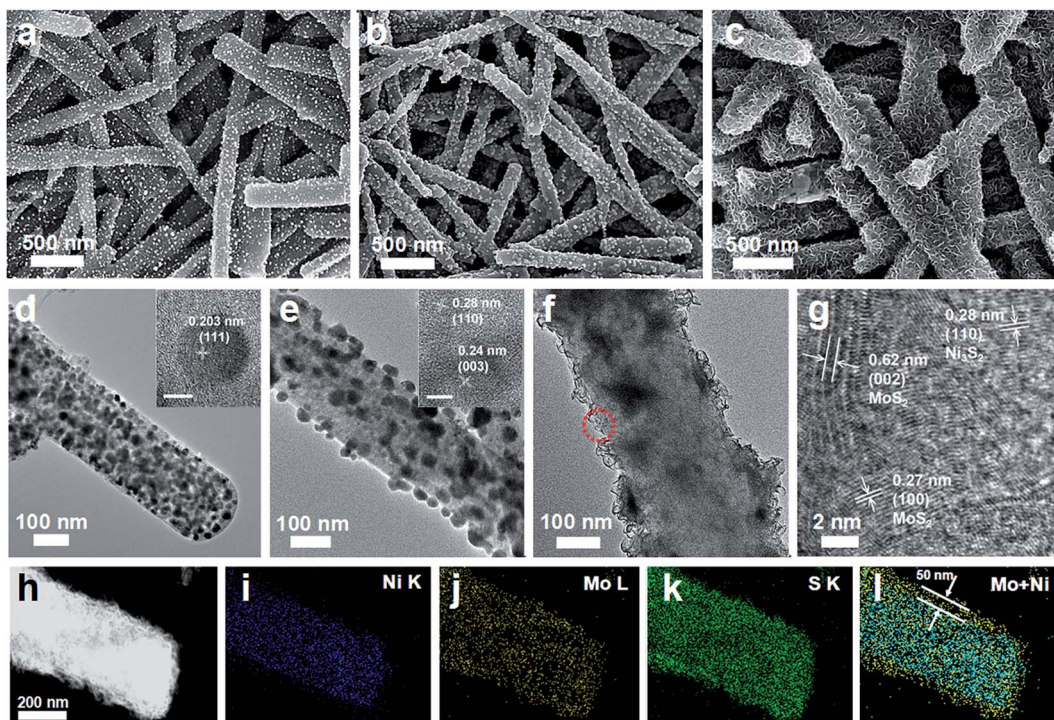


Fig. 3 FESEM and TEM images of (a & d) C/Ni-700 nanorods, (b & e) C@Ni₃S₂ core-shell nanorods, and (c & f) C@NM-700 double core-shell nanorods. (g) HR-TEM image of C@NM-700 nanorods obtained from the area highlighted in (f). (h-l) TEM image of a single C@NM-700 nanorod and its corresponding EDX elemental mapping of (i) Ni, (j) Mo, (k) S, and (l) Mo + Ni. Scale bar in the insets of (d and e): 5 nm.

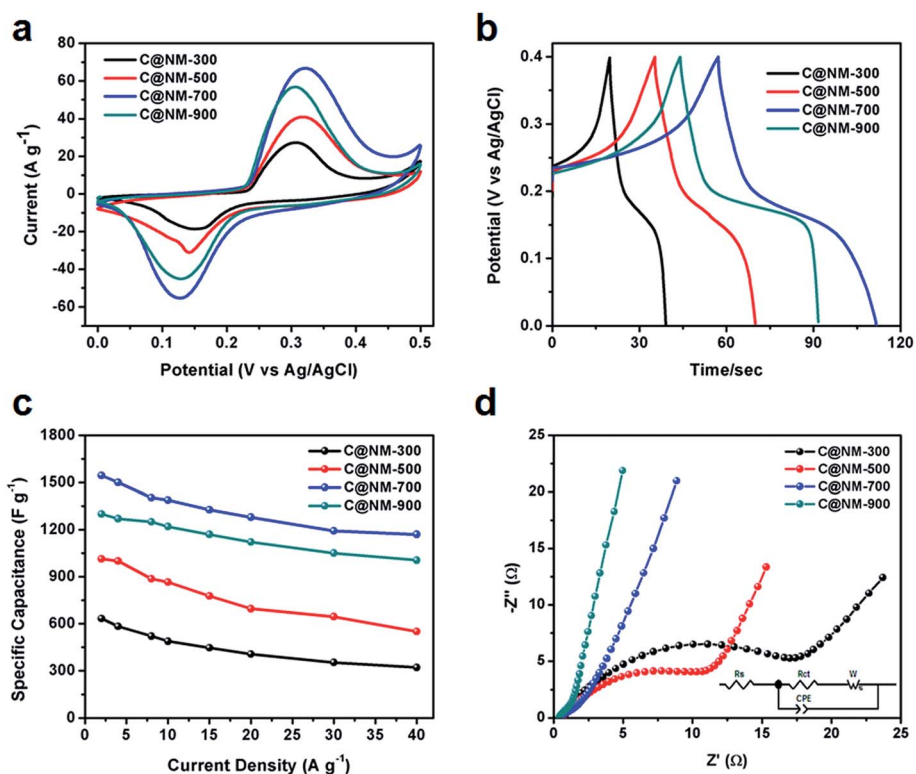


Fig. 4 Electrochemical performance of the C@NM-300, C@NM-500, C@NM-700, and C@NM-900 nanorod electrodes. (a) CV curves at a scan rate of 25 mV s⁻¹, (b) galvanostatic charge-discharge curves at a current density of 10 A g⁻¹, (c) current density dependent specific capacitance, and (d) the corresponding Nyquist plots.

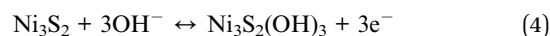
500, C@NM-700 and C@NM-900 is listed in Table S1.† It is obvious that the specific capacitance and rate capacity are greatly influenced by the core material in the core-shell nanorods. The rate capacity increases with increasing in carbonization temperature of the core C/Ni nanorods.

The enhanced electrochemical performance was further confirmed by the electrochemical impedance spectroscopy (EIS) measurements at equilibrium open circuit potential. Fig. 4d shows the Nyquist spectra of C@NM-300, C@NM-500, C@NM-700 and C@NM-900 electrodes in the frequency range from 100 kHz to 1 Hz. An equivalent circuit (inset in Fig. 4d), including an internal resistance (R_s), a constant phase element for the double layer capacitance (CPE), an interfacial charge transfer resistance (R_{ct}), and a Warburg resistance (W) from ion diffusion into the bulk of the electrode, was used to fit the experimental data.²⁵ In the high frequency region, the intercept to the x -axis represents the bulk resistance of the electrochemical system (R_s), while the semicircle can be assigned to the parallel combination of CPE and R_{ct} at the electrode-electrolyte interface.²⁶ The internal resistance R_s of C@NM-300, C@NM-500, C@NM-700, and C@NM-900 was measured to be 0.77, 0.68, 0.48, and 0.38 Ω , respectively, while their charge transfer resistance was 16.5, 11.2, 4.8, and 4.02 Ω , indicating that the C@NM-700 and C@NM-900 possessed much lower resistance than their counterparts synthesized from low-temperature graphitized C/Ni nanorods.

To unravel the relationship between the carbonization temperature and the electrochemical performance, a series of measurements were conducted to probe the C/Ni nanorods. Fig. 5 displays the Raman spectra of C/Ni-300, C/Ni-500, C/Ni-700 and C/Ni-900. The Raman spectrum in the range of 800–1900 cm^{-1} can be deconvoluted into four types of pristine carbon (inset of Fig. 5). The two main bands are the D (defect) and the G (graphite) bands. Additional bands are attributed to amorphous carbon and sp^3 carbon. The D band, which is located at about 1340 cm^{-1} , is attributed to the defect and lattice distortions in the carbon structure. The G band, at approximately 1580 cm^{-1} , results from the relative motion of sp^2 carbon (graphite) atoms.²⁷ The peak area ratio of the D band to G band (I_D/I_G) could be used as an indicator for the crystallinity of carbon.²⁸ As shown in Fig. 5, at low carbonization

temperatures (300 and 500 $^\circ\text{C}$), broad and rough Raman peaks are clearly observable, indicating the characteristic of amorphous carbon. As a result, the C/Ni-300 and C/Ni-500 showed a higher I_D/I_G ratio, 1.77 and 1.61, respectively, as compared to the C/Ni-700 and C/Ni-900 (1.50 and 1.14) in the Raman spectra. The decrease in the amorphous carbon peak (Fig. S5†) from C/Ni-300 to C/Ni-900 further demonstrated that the increase in carbonization temperature improved the material crystallinity. Higher graphitizability should endow the C/Ni nanorods with enhanced electrical conductivity,²⁹ which could benefit the charge transport in supercapacitors, leading to higher specific capacitance. Furthermore, high carbonization temperature could also help grow Ni nanoparticles on the external surface of C/Ni nanorods (Fig. 3a and S6a–c†), which later could be reacted with S^{2-} ions and converted to Ni_2S_3 . The growth of Ni nanoparticles could facilitate the full utilization of nickel to form Ni_3S_2 , thus resulting in higher pseudocapacitance. However, too high carbonization temperature (900 $^\circ\text{C}$) could cause agglomeration of Ni nanoparticles on C/Ni nanorods, which eventually led to decrease in capacitance.

To further highlight the importance of double core-shell nanostructures on the performance of supercapacitors, we compared the electrochemical properties between C@Ni₃S₂@MoS₂ double core-shell nanorods and C@Ni₃S₂ core-shell nanorods. Fig. 6a compares the CV curves of the C@Ni₃S₂ nanorods and C@Ni₃S₂@MoS₂ nanorods at a scan rate of 50 mV s^{-1} . The similar shape of the CV curves suggests the same reversible faradic reaction, resulting from the reversible redox reaction between Ni^{2+} and Ni^{3+} as described by the following equation:¹¹



The C@Ni₃S₂@MoS₂ nanorods display a larger enclosed area under the CV curve, indicating higher capacitance.³⁰ Fig. 6b shows the galvanostatic charge-discharge curves measured at a current density of 4 A g^{-1} , which displays a clear plateau, indicating the typical pseudocapacitive characteristics.³¹ Fig. 6c gives the corresponding specific capacitance obtained at different current densities. For the C@Ni₃S₂@MoS₂ double core-shell nanorods, a specific capacitance as high as 1544 F g^{-1} can be realized at a current density of 2 A g^{-1} , which is obviously larger than that of the C@Ni₃S₂ nanorods (1440 F g^{-1}). Furthermore, the C@Ni₃S₂@MoS₂ nanorods exhibit better rate capability than the C@Ni₃S₂ electrode. The enhanced electrochemical performance of the C@Ni₃S₂@MoS₂ nanorods should be attributed to the decoration of the interconnected MoS₂ nanosheets on the shell. MoS₂ was reported to show pseudocapacitive faradic charging only at low scan rates, when the diffusion process dominates.³² At low scan rates (below 25 mV s^{-1}), the charge/discharge process for the C@Ni₃S₂@MoS₂ nanorods is controlled by diffusion (refer to Fig. S7† for detailed calculations), which is able to offer some redox capacitance. At fast scan rates, MoS₂ nanosheets, which grow perpendicularly on the nanorods, can offer large surfaces for double-layer charge storage (BET surface area of C@Ni₃S₂@MoS₂ nanorods:

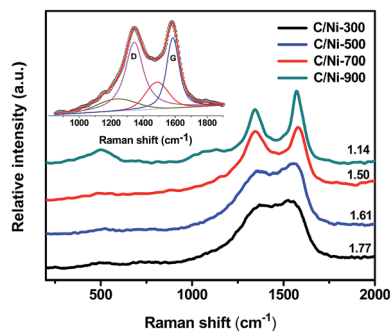


Fig. 5 Raman spectra of C/Ni-300, C/Ni-500, C/Ni-700, and C/Ni-900 nanorods. The inset shows the fitting diagram of C/Ni-700 nanorods.

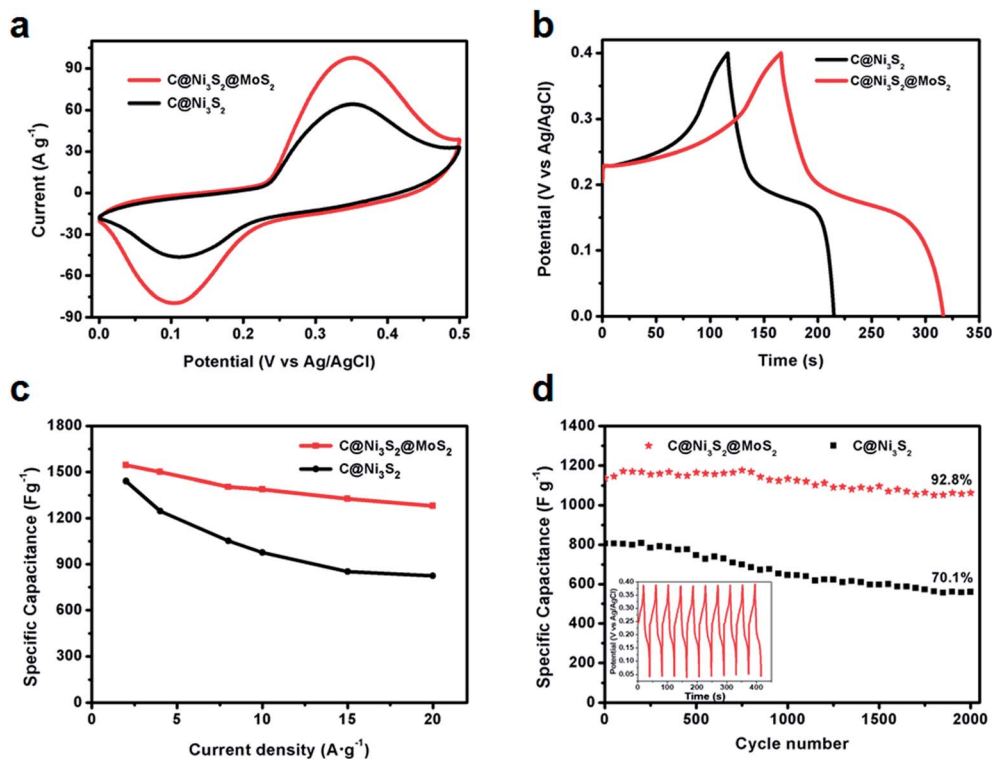


Fig. 6 Electrochemical performance of the C@Ni₃S₂@MoS₂ and C@Ni₃S₂ nanorod electrodes. (a) CV curves at a scan rate of 50 mV s⁻¹, (b) charge-discharge curves of C@Ni₃S₂@MoS₂ nanorods at a current density of 4 A g⁻¹, (c) specific capacitances obtained at different current densities, and (d) cycling performances of the C@Ni₃S₂ and C@Ni₃S₂@MoS₂ nanorods at a current density of 20 A g⁻¹ (the inset shows the last ten cycles of the charge-discharge curves of the C@Ni₃S₂@MoS₂ nanorods).

28.4 m³ g⁻¹ as compared with that of C@Ni₃S₂ nanorods: 16.2 m³ g⁻¹, Fig. S8†). Meanwhile, the interconnected MoS₂ shell combined with a highly conductive 1D carbon core allows for fast electrolyte diffusion and rapid electron transport, especially at high current densities. It is worth mentioning that the C@MoS₂ nanorods (Fig. S10†) exhibit much lower capacitance (319 F g⁻¹ at 2 A g⁻¹) as compared to that of the C@Ni₃S₂ and C@Ni₃S₂@MoS₂ nanorods, suggesting that most of the capacitance of C@Ni₃S₂@MoS₂ nanorods comes from Ni₃S₂ rather than MoS₂.

The durability of the electrode is also critical in practical applications. The cycling performance of the C@Ni₃S₂@MoS₂ and C@Ni₃S₂ nanorods at a current density of 20 A g⁻¹ is shown in Fig. 6d. Impressively, the C@Ni₃S₂@MoS₂ double core-shell nanorods show an outstanding capacitance retention of 92.8% after 2000 cycles. While for the C@Ni₃S₂ core-shell nanorods, only 70.1% of the initial capacitance remained. The inset in Fig. 6d shows the last ten charge-discharge curves of C@Ni₃S₂@MoS₂ nanorods, which are symmetrical with minimal variations, demonstrating excellent cyclability. Furthermore, for long-term cycling tests at a current density of 10 A g⁻¹, the C@Ni₃S₂@MoS₂ double core-shell nanorods maintained a high capacity retention of approximately 71.4% even after 10 000 cycles as shown in Fig. S11†. The better cycling performance of C@Ni₃S₂@MoS₂ nanorods could be attributed to the buffering of volume change by the interconnected MoS₂ nanosheets during the

charge-discharge processes. It is worth noting that the morphology and structure of the electrode can be well maintained after long-term charging-discharging cycles (Fig. S12†). Electrochemical impedance spectroscopy was further applied to study the electrochemical performance (Fig. S13a†). The C@Ni₃S₂@MoS₂ nanorods show a larger slope in the low frequency regions indicating better capacitive behavior with lower diffusion resistance.³³ In addition, the nearly unchanged EIS curves obtained before and after 2000 charge-discharge cycles (Fig. S13b†) further demonstrate the excellent stability of the C@Ni₃S₂@MoS₂ nanorods. As summarized in ESI Table S2,† the electrochemical performance of our C@Ni₃S₂@MoS₂ nanorods has been greatly improved as compared with those of recently reported Ni₃S₂- and MoS₂-based materials, especially the rate performance. Therefore, the C@Ni₃S₂@MoS₂ nanorods can be a good candidate as high-performance supercapacitors.

4. Conclusion

In summary, hierarchical C@Ni₃S₂@MoS₂ double core-shell nanorods were successfully designed and synthesized by a simple hydrothermal method using highly conductive C/Ni nanorods as both the template and nickel source. The C@Ni₃S₂@MoS₂ double core-shell nanorods exhibited high specific capacitance, excellent rate capability, and good cycling stability for supercapacitors, thanks to the good electron conductivity

offered by the carbon backbone core and large accessible surfaces induced by the MoS₂ shell. Our work could provide a general and promising approach to fabricate double core-shell nanostructures for energy storage applications.

Acknowledgements

This work was supported by the Nanyang Technological University startup grant (M4080977.120), Singapore Ministry of Education Academic Research Fund (AcRF) (Tier 1: M4011021.120), the National Research Foundation (NRF), Prime Minister's Office, Singapore under its Campus for Research Excellence and Technological Enterprise (CREATE) program, Program for New Century Excellent Talents in University (NCET-13-0853), Qing Lan Project, Synergetic Innovation Center for Organic Electronics and Information Displays, the Priority Academic Program Development of Jiangsu Higher Education Institutions (PAPD).

References

- 1 P. Simon and Y. Gogotsi, *Nature*, 2008, **7**, 845–854.
- 2 M. Winter and R. J. Brodd, *Chem. Rev.*, 2004, **104**, 4245–4269.
- 3 B. E. Conway, *J. Electrochem. Soc.*, 1991, **138**, 1539–1548.
- 4 G. P. Wang, L. Zhang and J. J. Zhang, *Chem. Soc. Rev.*, 2012, **41**, 797–828.
- 5 S. J. Peng, L. L. Li, H. T. Tan, R. Cai, W. H. Shi, C. C. Li, S. G. Mhaisalkar, M. Srinivasan, S. Ramakrishna and Q. Y. Yan, *Adv. Funct. Mater.*, 2014, **24**, 2155–2162.
- 6 J. Yang, Y. F. Zhang, C. C. Sun, G. L. Guo, W. P. Sun, W. Huang, Q. Y. Yan and X. C. Dong, *J. Mater. Chem. A*, 2015, **3**, 11462–11470.
- 7 Y. F. Zhang, M. Z. Ma, J. Yang, C. C. Sun, H. Su, W. Huang and X. C. Dong, *Nanoscale*, 2014, **6**, 9824–9830.
- 8 D. Li, X. W. Li, X. Y. Hou, X. L. Sun, B. L. Liu and D. Y. He, *Chem. Commun.*, 2014, **50**, 9361–9364.
- 9 S. B. Ni, X. L. Yang and T. Li, *Mater. Chem. Phys.*, 2012, **132**, 1103–1107.
- 10 W. J. Zhou, X. H. Cao, Z. Y. Zeng, W. H. Shi, Y. Y. Zhu, Q. Y. Yan, H. Liu, J. Y. Wang and H. Zhang, *Energy Environ. Sci.*, 2013, **6**, 2216–2221.
- 11 D. Z. Kong, C. W. Cheng, Y. Wang, J. I. Wong, Y. P. Yang and H. Y. Yang, *J. Mater. Chem. A*, 2015, **3**, 16150–16161.
- 12 W. D. Yu, W. R. Lin, X. F. Shao, Z. X. Hu, R. C. Li and D. S. Yuan, *J. Power Sources*, 2014, **272**, 137–143.
- 13 Z. C. Xing, Q. X. Chu, X. B. Ren, C. J. Ge, A. H. Qusti, A. M. Asiri, A. O. Al-Youbi and X. P. Sun, *J. Power Sources*, 2014, **245**, 463–467.
- 14 T. Zhu, H. B. Wu, Y. B. Wang, R. Xu and X. W. Lou, *Adv. Energy Mater.*, 2012, **2**, 1497–1502.
- 15 H.-Y. Wang, F. X. Xiao, L. Yu, B. Liu and X. W. Lou, *Small*, 2014, **10**, 3181–3186.
- 16 D. P. Cai, H. Huang, D. D. Wang, B. Liu, L. L. Wang, Q. H. Li and T. H. Hong, *ACS Appl. Mater. Interfaces*, 2014, **6**, 15905–15912.
- 17 Y. Zhang, W. P. Sun, X. H. Rui, B. Li, H. T. Tan, G. L. Guo, S. Madhavi, Y. Zong and Q. Y. Yan, *Small*, 2014, **11**, 3694–3702.
- 18 X. Bo, L. Zhu, G. Wang and L. Guo, *J. Mater. Chem.*, 2012, **22**, 5758–5763.
- 19 Z. M. Wan, J. Shao, J. J. Yun, H. Y. Zheng, T. Gao, M. Shen, Q. T. Qu and H. H. Zheng, *Small*, 2014, **10**, 4975–4981.
- 20 F. H. Bai, Y. D. Xia, B. L. Chen, H. Q. Su and Y. Q. Zhu, *Carbon*, 2014, **79**, 213–226.
- 21 K. Q. Zhou, S. H. Jiang, C. L. Bao, L. Song, B. B. Wang, G. Tang, Y. Hu and Z. Gui, *RSC Adv.*, 2012, **2**, 11695–11703.
- 22 S. Kalluri, K. H. Seng, Z. Guo, A. Du, K. Konstantinov, H. K. Liu and S. X. Dou, *Sci. Rep.*, 2015, **5**, 11989.
- 23 D. W. Yu and T. A. Utigard, *Thermochim. Acta*, 2012, **533**, 56–65.
- 24 Z. Chen, D. S. Yu, W. Xiong, P. P. Liu, Y. Liu and L. M. Dai, *Langmuir*, 2014, **30**, 3567–3571.
- 25 L. Wang, Z. H. Dong, Z. G. Wang, F. X. Zhang and J. Jin, *Adv. Funct. Mater.*, 2013, **23**, 2758–2764.
- 26 K.-P. Wang and H. Teng, *J. Electrochem. Soc.*, 2007, **154**, A993–A998.
- 27 P. K. Chu and L. H. Li, *Mater. Chem. Phys.*, 2006, **96**, 253–277.
- 28 J. Long, X. Q. Xie, J. Xu, Q. Gu, L. M. Chen and X. X. Wang, *ACS Catal.*, 2012, **2**, 622–631.
- 29 D. D. L. Chung, *J. Mater. Sci.*, 2004, **39**, 2645–2661.
- 30 J. Yan, Z. Fan, W. Sun, C. Ning, T. Wei, Q. Zhang, R. Zhang, L. Zhi and F. Wei, *Adv. Funct. Mater.*, 2012, **22**, 2632–2641.
- 31 Z. Tang, C. H. Tang and H. Gong, *Adv. Funct. Mater.*, 2012, **22**, 1272–1278.
- 32 J. M. Soon and K. P. Loh, *Electrochem. Solid-State Lett.*, 2007, **10**, A250–A254.
- 33 L. J. Han, P. Y. Tang and L. Zhang, *Nano Energy*, 2014, **7**, 7367–7372.